Calibrated suspended sediment observations during large amplitude non-linear internal waves

W. C. Edge[1], **N. L. Jones**[1], **M. D. Rayson**[1], **G. N. Ivey**[1]

[1]Oceans Graduate School, University of Western Australia, Perth, Western Australia, Australia

Key Points:

- Observations of sediment mobilisation and transport in the benthic bottom boundary layer under non-linear internal waves.
- Comparison of two calibration approaches and inference of suspended sediment concentration from acoustic and optical instruments.
- Bayesian calibration approach adopted to quantify the uncertainty of different calibration methods and instruments.

Corresponding author: W. C. Edge, william.edge@research.uwa.edu.au

Abstract

While it has been recognized for some time that large-amplitude nonlinear internal waves (NLIW) can mobilise and transport sediment, quantitative observations of this process are rare. Rarer still are accompanying measurements or even estimates of suspended sediment mass concentration (SSC) during the passage of NLIW. Here we present high resolution observations of NLIW and the SSC response within the bottom boundary layer. The observations were made in 2017 in the Browse Basin on Australia's Northwest Shelf in 250 m of water. We compare two direct calibration methods designed to overcome the inherent difficulty of directly observing SSC in deeper ocean environments, and employ Bayesian methods to estimate the uncertainty in SSC. Both calibration methods were used as bench-marking to infer SSC from a range of instrumentation deployed on a bottom-lander frame (acoustics, optical, and laser scattering). Estimates of near-bed SSC, with uncertainty, during NLIW passages are presented for each instrument. During a large NLIW event, the peak mean SSC estimate was 102 mg L^{-1} with 95% credible intervals of 93 and 112 mg L^{-1}, 0.87 m above the sea bed. We also examine the propagation of uncertainty to several derived quantities, such as SSC gradients. This work is the first step towards the quantitative analysis of sediment dynamics needed to develop parameterized models associated with the passage of NLIW.

Plain Language Summary

Internal waves can travel through the ocean and have the potential to generate significant currents as they move into shallow water on the continental shelf. This process can lift and transport local sea bed sediment if the near-bed currents are strong enough. This process is short-lived, unpredictable, and generally occurs in deeper waters, making high quality observations rare. We present high resolution observations of ocean currents and the sediment response during the passage of large internal waves. The observations were captured using a bottom-lander frame deployed on the Northwest Shelf of Australia for two months in 2017. We used acoustic, optical, and laser scattering instruments to measure suspended sediment properties. These data sets were converted to estimates of suspended sediment mass concentration by calibration. We performed the calibrations using Bayesian inference, a statistical technique that allows for straight-forward uncertainty estimation. This work is a first step towards modelling of sediment transport with uncertainty.

1 Introduction

Sediment mobilisation and transport on continental slopes and shelves are under-observed phenomena that have important consequences for nutrient and pollutant redistribution, cross-shelf particle fate, and sea bed infrastructure design, construction, and maintenance. It has long been known that energetic internal waves exist throughout the world's oceans, yet only in the last 30 years have researchers begun to capture with sufficient temporal resolution the sporadic resuspension events driven by internal waves (e.g., Churchill et al., 1988; Gardner, 1989). Recent observations and theory suggest that in the shelf environment internal waves may be the key contributor to both instantaneous sediment resuspension (Butman et al., 2006; Bonnin et al., 2006) and to the long-term geomorphology (Cacchione et al., 2002).

Tidally-generated internal waves transport energy throughout the ocean away from their source regions (Zaron, 2019). Given the right conditions, these waves steepen to form non-linear internal waves (herein NLIW), examples of which have been observed at our site in around 250 m of water on the continental northwest shelf (NWS) of Australia (Rayson et al., 2019). As these propagating waves encounter shallower water they shoal and break, resulting in intensified currents and turbulence near the sea bed (Jones

et al., 2020; Zulberti et al., 2020). This process has been shown to resuspend (Valipour et al., 2017), transport (Noble & Xu, 2003; Hosegood et al., 2004; Cheriton et al., 2014), and even fully detach sediment from the near-bed region (Moum et al., 2002; McPhee-Shaw et al., 2004). See the review by Boegman and Stastna (2019) for a thorough description.

Observations of mixing and sediment resuspension by NLIW have led to hypotheses on how this may influence chemical and biological processes in shelf seas, lakes, and estuaries (Cacchione & Drake, 1986; Klymak & Moum, 2003; Valipour et al., 2017). Based on observed dissipation levels, Sandstrom and Elliott (1984) proposed that several internal waves per tidal cycle may be sufficient to supply nutrients from the sediment throughout the water column. Churchill et al. (1988) investigated the hypothesis that internal waves sorted shelf sediments and resulted in a fine sediment sink on the slope, although conclusive evidence for this process was not observed. Concern over the ability of fine sediments to redistribute pollutants from the bed into the water column and other areas of the ocean has also motivated studies (e.g., Bogucki et al., 1997; Gardner, 1989). On the NWS in particular, the expansion of offshore infrastructure has also raised questions related to sea bed infrastructure stability and sub-sea operation visibility.

A detailed analysis of NLIW-induced sediment resuspension requires near-bed observations with sufficient temporal and vertical resolution. In the bottom boundary layer (BBL) of shelf seas it is difficult to directly observe SSC with high resolution. To overcome this challenge we deploy a range of instrumentation (acoustics, optical, and laser diffraction) that each measure some indirect characteristic of sediment in suspension, with the expectation of proportionality to suspended sediment mass concentration (SSC). In general, the researcher is responsible for converting these indirect measurements of SSC through calibration (e.g., Puig et al., 2001; Fugate & Friedrichs, 2002), or more often, just present the observations as the raw parameter, e.g. acoustic backscatter intensity. Although presentation of the raw data may avoid the addition of potential calibration model errors or biases, it can lead to a discrepancy or divergence between observations and modelling that limits quantitative comparison.

Calibration requires concurrent measurements (in both time and space) of direct (true) SSC with indirect observations. We performed and compared two popular calibration methods: *in-situ* field calibration achieved by vertical profiling a package with both an instrument and Niskin water bottles; and *laboratory* calibration occurring post-deployment using sediment collected from the sea floor. Both approaches introduce uncertainty, through the calibration model itself and through the limitations of the method employed. This uncertainty can be represented by the variance of the calibration model parameters (or indeed any model parameters).

Sediment resuspension is parameterized in sediment transport models and uncertainty in this parameterization should be included for best modelling outcomes. In addition, many of the variables used to model sediment transport are better represented by probabilistic objects rather than single values. Adequate representation of the resulting cumulative uncertainty in sediment transport models is a key research challenge. Uncertainty can arise from physical variability, sampling strategy, measurement error, and model selection (Schmelter et al., 2011). For this work we have employed Bayesian inference, a technique for statistical parameter estimation that computes the posterior distribution of the model parameters, that is then used directly to quantify uncertainty (Gelman et al., 2013).

Calibration of indirect measurements of SSC with an estimate of uncertainty is a key first step towards understanding sediment transport and creating relevant models. In addition, the techniques used here explicitly estimate noise levels of different instruments and sampling strategies. Typical data fitting approaches fail to meaningfully quantify uncertainty and the implications for further analysis, e.g., when calculating an SSC

gradient (in time or space), the turbulent SSC fluxes, or the position of SSC isopleths. By using Bayesian inference to estimate calibration parameters as fully probabilistic objects, we can create a coherent framework to propagate uncertainty through one or more models in order to accurately compute the probability distribution of a single quantity of interest.

1.1 Objectives and outline

The primary aims for this paper are: first, to present and evaluate two calibration methods (*in-situ* and *laboratory*); second, use a coherent framework to connect our many indirect measurements of SSC with a relatively small sample of direct measurements; and finally, to demonstrate the utility and benefits of this approach to near-bed SSC observations of NLIW.

The methodology described herein is able to connect many indirect observations of SSC together by using each calibrated instrument, in turn, as the "truth" for a new calibration. These chained calibrations could be done by using concurrent measurements (in height and time) from instruments deployed on a bottom-lander mooring. This approach allows us to connect sparse (and difficult to obtain) direct measurements of SSC with large indirect observational data sets, using Bayesian methods to keep track of uncertainty.

We start by reviewing some relevant concepts on indirect SSC measurement (Section 2) and summarise some key Bayesian concepts (Section 3). We then describe the field experiment (Section 4), the calibration approach (Section 5), and the results (Section 6). Finally, we show estimates of near-bed SSC with uncertainty from multiple instruments collecting observations during the propagation of two NLIW (Section 7).

2 Measuring suspended sediment concentration

2.1 Optical backscatter

An optical backscatter instrument (OBS) functions by projecting a beam of light into the water and measuring the amount of light reflected back to a sensor. The sensor effectively measures the total cross-sectional area of all particles within the measurement volume, which Fugate and Friedrichs (2002) showed is proportional to the volume concentration and inversely proportional to the particle diameter. It has been well demonstrated that, at relatively low concentrations, when the particle size distribution (PSD) in suspension remains constant, a linear relation exists between the OBS output and SSC (Green & Boon, 1993).

In practice, the observed PSD in suspension is rarely constant in time and changes will influence the output. Ludwig and Hanes (1990) found that the OBS response increased by approximately one order of magnitude from sand to mud, and Gibbs and Wolanski (1992) found that when observing fine sediment, increasing mean flow speed increased OBS response by about a factor of two owing to dynamic floc breakup (and vice versa). As a result, an OBS calibration may give poor estimates of SSC when the observed PSD varies in time.

2.2 Laser scattering

Laser scattering provides a measurement of PSD by recording the angular intensity of laser beam light as it is scattered by particles suspended within the beam path. The LISST 200-X (Sequoia Scientific, Inc.) is a laser scattering instrument designed to measure PSD in-situ at high temporal resolution (up to 1 Hz). The LISST supplies a volume concentration, C_V, over 36 particle size bins ranging from 1–500 µm.

The LISST is able to measure both individual particles and flocs in suspension, but it cannot distinguish between them because it characterizes each floc as a single particle (Mikkelsen et al., 2005). A collection of fine cohesive particles that has aggregated into a floc will thus be seen as a single large particle with a volume many times greater than the sum of its parts. Hence, observations of dynamic aggregation and breakup driven by varying background flow can exert significant influence over the measured volume concentration, C_V.

Mikkelsen and Pejrup (2001) showed that when observing flocs, SSC and C_V are approximately related by the effective density, $\Delta\rho$:

$$\rho_{floc} - \rho_{water} \approx \Delta\rho \approx \frac{SSC}{C_V}. \tag{1}$$

When both flocs and single particles are present, SSC/C_V is the weighted average of the single particle density and $\Delta\rho$, and thus equation 1 is no longer valid. Thus, a linear relationship between SSC and C_V should perform well when $\Delta\rho$ is relatively constant, and poorly when it is not. Additional limitations exist for this type of instrument, as summarised by Fugate and Friedrichs (2002).

2.3 Acoustic backscatter

Acoustic instruments, such as acoustic Doppler velocimeters (ADVs) and acoustic Doppler current profilers (ADCPs), observe particles in suspension in a manner analogous to OBS instruments. Particles in the measurement volume scatter an acoustic signal emitted from the instrument, a portion of which is reflected back to a receiver. For a given particle, acoustic scattering is dictated by the particle form function and particle scattering cross-section, where the form function itself is a complex function primarily of particle size and density, and other variables such as shape and elasticity (Thorne & Hurther, 2014).

When the particle population remains constant, the ensemble averaged form function is also constant, and an empirical relationship between backscatter strength and the base 10 logarithm of SSC can be found across a wide range of environmental conditions (e.g. Fugate & Friedrichs, 2002; Gartner, 2004; Ha et al., 2009). At relatively low concentrations (less than 1 g L^{-1}), this relationship is

$$log_{10}(SSC) = mBS + b, \tag{2}$$

where BS is the measured backscatter. The acoustic log_{10} decibel scale introduces complications for uncertainty estimation that are examined in the results.

As with the OBS and LISST instruments, changes to both the observed primary PSD and flocculation processes can influence an acoustic instruments response. For example, MacDonald et al. (2013) showed through controlled laboratory experiments that the flocculation process significantly alters the acoustic scattering properties of cohesive sediment.

3 Bayesian inference

3.1 Bayes theorem

Bayesian inference is a statistical modelling approach that accommodates probabilistic objects and is well suited to environmental data analysis (e.g., Schmelter et al., 2011; Manderson et al., 2019). It does this by drawing conclusions about model parameters given some set of observed data, using Bayes' rule.

Measurement of a probabilistic process produces a set of observations, X and y; for example, OBS data and SSC from filtered water samples. The y data are conditioned

on both X and the model parameters, represented by the vector θ. This is called the *likelihood function*, $p(y|X,\theta)$, which describes the probability of the y data having a particular value given θ and some observations X. In the Bayesian paradigm, θ is unknown and not fixed. The probability of θ, $p(\theta)$, is called the *prior* distribution and represents any initial knowledge about θ (and can be vague, non-informative, or include expert knowledge, for example). Bayes' theorem states that the *posterior* distribution, $p(\theta|X,y)$, depends upon both the prior distribution and the likelihood function (Gelman et al., 2013),

$$p(\theta|X,y) = \frac{p(\theta)p(y|X,\theta)}{p(y)}, \tag{3}$$

where $p(y)$ is a normalising constant that is the sum over all possible values of θ.

Model uncertainty can be extracted from the posterior distribution, making it trivial to derive an unambiguous, calculable definition of uncertainty, e.g. the credible intervals (CI). A common presentation of uncertainty is the 0.95% CI, e.g. intervals (a,b) that indicate $p(a < \theta < b|X,y) = 0.95$, or the 95% highest probability density of the posterior distribution (e.g. Manderson et al., 2019).

3.2 Linear calibration model

In the Bayesian paradigm, for the case of a two parameter linear model $f(x) = mx+b$ (such as our OBS and SSC observations), θ contains all model parameters, the slope and intercept in $\beta = \begin{bmatrix} b \\ m \end{bmatrix}$, and the residual variance parameter, σ. The parameter σ represents the range of possible values the y residuals could be, given the distribution of possible slope and intercept values. The observed data are represented by the matrix X (OBS) and the vector y (SSC), so the model takes the vector form,

$$y|\beta,\sigma,X \sim \mathcal{N}(X\beta,\sigma^2 I). \tag{4}$$

Here I is the $n\times n$ identity matrix (for n observations). $\mathcal{N}()$ indicates a normal distribution with a mean and variance in the brackets, so that each SSC data point (y_i) is a distribution with a mean, $X_i\beta$, and a variance, σ^2. This form of the model assumes equal uncertainty for each y value, Gaussian white noise for the y residuals with a constant variance (homoscedasticity) and zero conditional correlations. More complex models are possible but were not considered here.

3.3 Model setup & computation

The Python software package *PyMC3* was used to calculate the posterior distribution of the calibration model parameters. First, prior distributions must be specified for each model parameter, regardless of the computational method. *PyMC3* contains a significant library of distributions that make it trivial to specify priors.

For the linear model proposed, priors for β were simply specified as normal distributions, and σ was specified as half-normal (the distribution of the residual parameter represents the absolute value of the residuals and cannot be negative). Each prior can be specified with large variance so as to be effectively non-informative, in which case the posterior distribution is "weighted" by the data. The model setup can be intuitively viewed using a directed acyclic graph (Figure 1).

Our aim is to estimate the joint posterior distribution for the model parameters, $p(\beta,\sigma|X,y)$, through a sampling algorithm. Given a data set, Markov Chain Monte Carlo (MCMC) sampling can be used to determine the posterior distribution for the slope and intercept in β, and the corresponding residual variance, σ^2. These individual posterior distributions combine to form the joint posterior distribution used to estimate total uncertainty. More information on the MCMC sampling algorithm can be found in Salvatier et al. (2016).

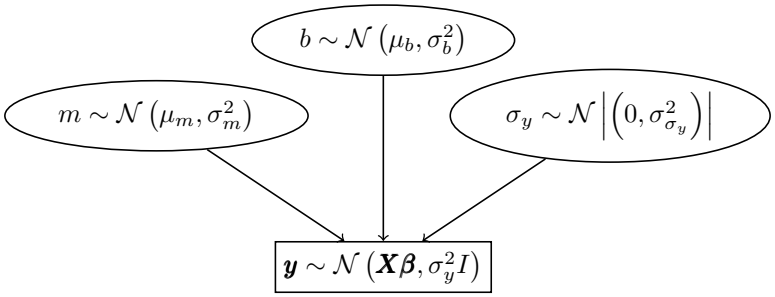

Figure 1. Directed acyclic graph of a single linear model. Prior distributions (shown as ellipses) inform the linear model (rectangle).

4 Site description

4.1 Field experiment

The field data came from the Kimberley Internal Solitons Sediment and Mixing Experiment (KISSME 2017). The experiment was undertaken from 1 April to 22 May 2017 on Australia's NWS in around 250 m of water. The region is characterised by a 200 km wide continental shelf and a large tidal range. The measurement site was chosen for its relatively flat bathymetry, with an estimated cross-shelf slope of 0.2% for at least 40 km in all directions (Figure 2). For this work we restrict our analysis to the 15 days from 2 to 16 April when all instruments had power and performed as expected.

A triangular arrangement of three through-water-column (TWC) moorings about 500 m apart and a separate bottom lander frame were deployed (Figure 2ii) to measure vertical and horizontal variability of internal wave-affected ocean properties, as detailed in Rayson et al. (2019). The focus for this study was the data collected from the bottom-lander mooring, located approximately 100 m south of the nearest TWC mooring. The lander was specifically designed to capture the BBL response to NLIW forcing (Figure 3). The nearest TWC mooring captured temperature data at approximately 10 m vertical resolution, sampling at 2 Hz and averaged to 60 s, which was used to provide additional context to the lander observations.

A shipboard frame was vertically profiled as close as possible to the lander mooring for two 12-hour periods. The two periods were chosen to represent spring and neap tide conditions. Profiles were done at hourly intervals (currents permitting), but some profiles were obtained at distances of up to 1,400 m from the lander mooring because of strong currents and mooring interference concerns. Attached to the profiling frame were 12 Niskin bottles, a CTD, transmissometer, and a LISST 200-X that auto-logged to the ships computer. Bottle samples were collected during both profiling periods and vacuum-filtered on-board (Figure 2ii). A bottom sediment sample was collected from the sea bed surface using a Smith McIntyre grab, which indicated a mean diameter of 21 μm. Further details regarding collection, processing, and PSD analysis are summarised separately (Appendix A).

4.2 Site dynamics

Baroclinic motion in the form of an internal tide was observed in the TWC temperature record throughout the deployment, with increased amplitude during spring tides (Rayson et al., 2019). NLIW of depression with amplitudes up to 70 m propagated past the moorings in the first few days of the deployment, just after the peak barotropic spring tide, generating strong near-bed currents and elevated SSC (e.g., at 0.87 m ASB). The

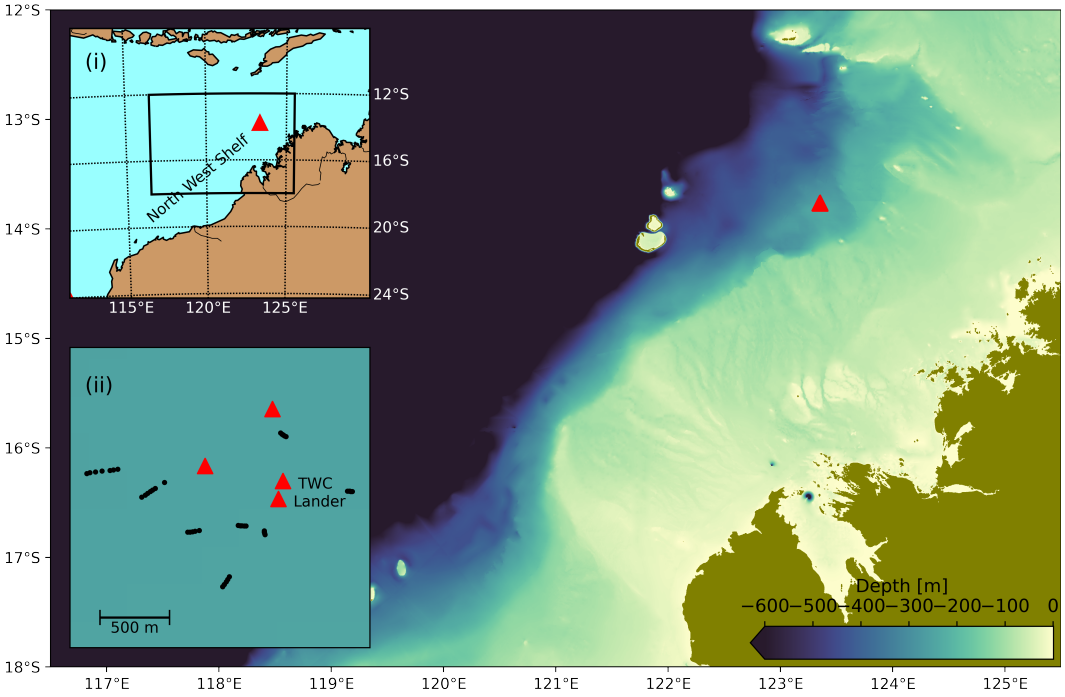

Figure 2. Location of the KISSME 2017 field campaign (red triangle) on the NWS of Australia. Inset (i) shows the regional location between mainland Australia and the Indonesian archipelago to the north. Inset (ii) details of the mooring configuration, with black dots showing the location of all Niskin bottle samples used for the in-situ calibration.

waves propagated southeast towards the coast, approximately cross-shelf, with near-bed currents directed offshore.

Peak barotropic tidal velocity was approximately 0.4 m s^{-1} and tidal range was about 4 m. The maximum current speed driven by baroclinic motions was estimated at 0.6 m s^{-1} at 20 m above sea bed (ASB) during the largest NLIW events (Zulberti et al., 2020). Baroclinic amplitude reduced significantly during the following neap tide and began to increase again as the barotropic tidal range increased. During the second spring tide, however, baroclinic motion was more linear and peak amplitudes and near-bed baroclinic induced currents were significantly less than during the first spring period.

4.3 Instrumentation and data processing

The lander was equipped with two ADVs, an upward looking ADCP, an OBS, and a LISST (as per the configuration in Figure 3). The two 6 MHz ADVs were located at 0.49 and 1.41 m ASB and sampled at 64 Hz. The 1 MHz ADCP sampled over the depth range from 0.53 to 23.35 m ASB at 0.2 m vertical resolution and at 8 Hz. The LISST 200-X sampled every 12 s at 0.87 m ASB, and the OBS collected a three-sample burst every 90 s at 1.14 m ASB (Table 1).

The *in-situ* calibration data sets from the deployed instruments were produced by taking the mean over 5-minute blocks for the 15 day record. This was done to reduce the influence of spatial variation between each instrument and to average over several of the longest turbulent fluctuations expected, whilst limiting the inclusion of internal wave fluctuations. The observation data was processed by averaging over the 5-minute blocks but at 1-minute intervals (i.e. 5-minute boxcar-filtering centred on a 1-minute time

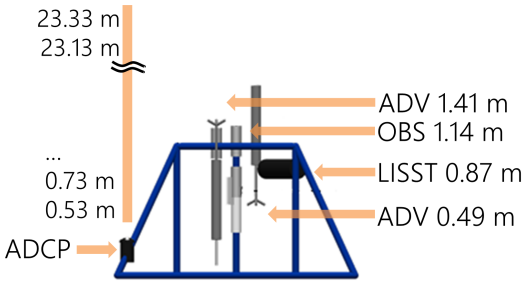

Figure 3. Schematic of the KISSME 2017 bottom lander setup showing the measurement volume height above the sea bed for each instrument. Note that the vertical fifth beam of the ADCP was used for backscatter.

Table 1. KISSME 2017 instrument sampling programs

Instrument	Sampling frequency	Height (m ASB)
LISST	12 s	0.87
OBS	90 s	1.14
ADCP	8 Hz	0.53–23.33 (0.2 m spacing, 115 bins)
ADV	64 Hz	0.49 and 1.41
TWC thermistors	2 Hz	∼10 m spacing

step, giving an 80% overlap), rather than the non-overlapping blocks used for the calibration models. The same flagging process was used for both data sets.

The LISST was processed using the manufacturer supplied software and instructions. Warning flags were included in the data set, but bad flags were not, and only blocks with at least 80% good data return were included for subsequent analysis. The LISST data was also used to identify periods of flocculation (described next). Raw voltage data from the OBS was converted to units of NTU using the latest manufacturer calibration parameters and the median value from each burst was selected. Data points where the instrument reached its upper limit were flagged and removed. Spikes from the OBS instrument that occurred towards the end of the deployment were visually removed, and only 5-minute blocks with at least two (out of three) data points were included.

Echo intensity (EI) from each ADV was left as counts for simplicity, under the assumption that changes in water and particle attenuation were insignificant for a point measurement. Only one beam from each ADV was used and no flags were applied. The final EI time series from each ADV was inspected visually and some suspect spikes from the upper ADV data set were visually flagged and removed.

ADCP EI was automatically converted to uncorrected backscatter (in dB) during processing with the manufacturer software. Backscatter from beam 5 (vertical) was corrected using the method described by Gartner (2004), including the near-field correction. TWC temperature data was used to calculate variable water attenuation vertically and temporally (with constant salinity and pressure). Viscous and scattering attenuation by sediment particles in suspension was assumed to be insignificant based on the ADCP operating frequency, bed sample PSD, and relatively low peak concentration values. ADCP receiver saturation was identified and flagged during the calibration process (described in Section 5). Unfiltered data with flags applied (except ADCP saturation) is presented for an example 24-hour period (Figure 4).

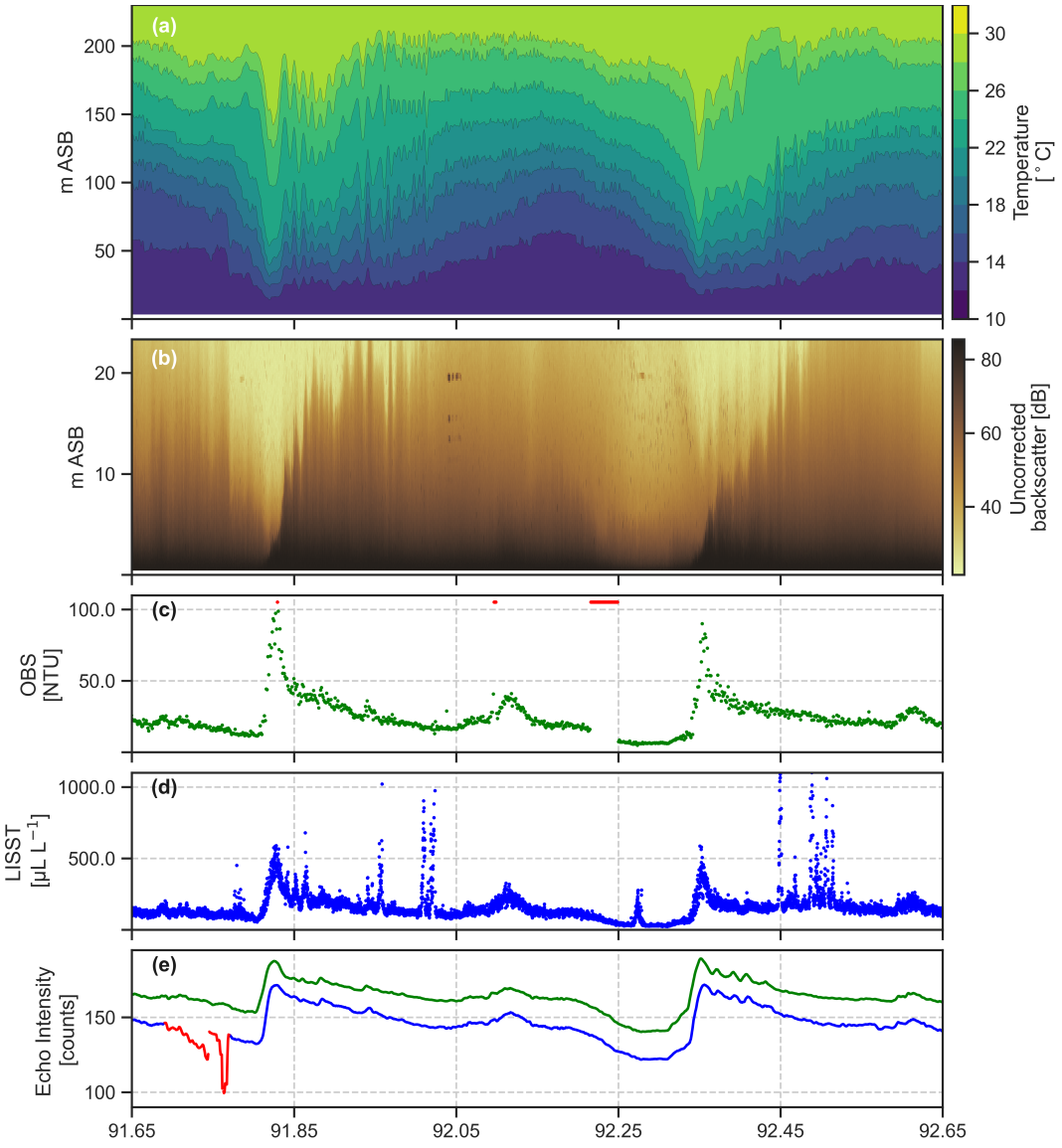

Figure 4. Example 24-hour period showing data from the KISSME 2017 field experiment; (a) TWC temperature from SP250, (b) uncorrected ADCP backscatter at 8 Hz and 0.2 m vertical resolution (saturation not flagged), (c) OBS data at 90 s, (d) LISST total volume concentration data at 12 s flagged as per manufacturer's instructions, and (e) boxcar-filtered echo intensity for the lower (green) and upper (blue) ADV. Flagged data is either red or orange.

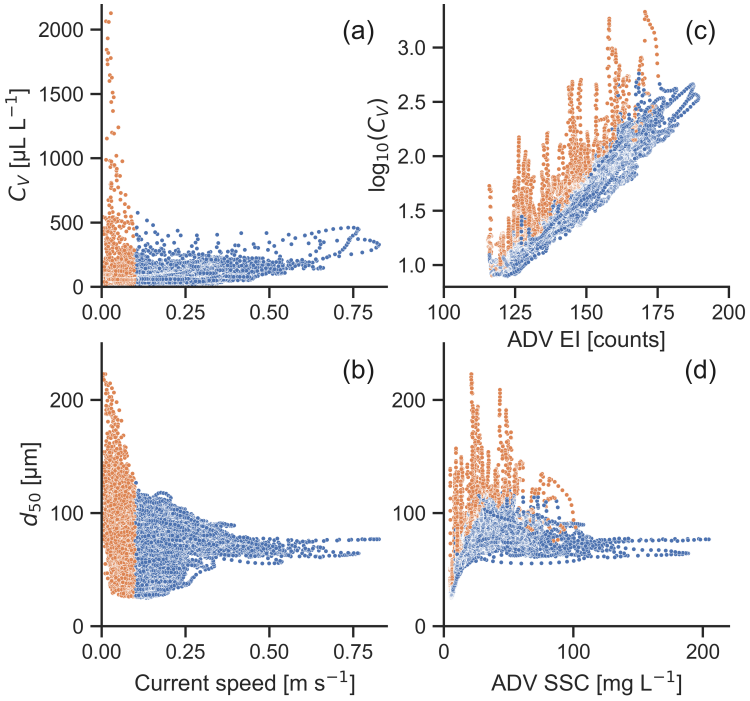

Figure 5. LISST data with other variables to identify instances of flocculation. C_V and d_{50} are total volume concentration and mean diameter from the LISST, respectively. Orange points represent times when the 5-minute mean current speed was less than 0.1 m s^{-1}, and blue is the rest of the data. Unlabelled axes are shared.

4.3.1 Additional LISST data quality control

Further investigation of the processed LISST data revealed spikes in C_V, particle size, and attenuation that were not readily explainable by the physical forcing. In addition, the spikes never registered via the acoustic or optical backscatter instruments. Comparison of C_V and d_{50} to current speed indicated that the spikes only occurred during calm conditions (Figure 5a,b). Data points where the 5-minute mean current speed was less than 0.1 m s^{-1} were flagged (4.1% of total data). Although flocculation is primarily controlled by the magnitude of turbulence dissipation (Hoitink & Hoekstra, 2005), a current speed flag proved to be a simple and effective method of identifying rapid floc growth.

Comparison of $log_{10}(C_V)$ with EI from the lower ADV showed that this flag effectively captured the deviations away from the expected linear relationship (Figure 5c). Whenever current speed was below the threshold, particle size would grow (regardless of prior particle size), and this process would continue until current speed increased again. In contrast, when current speed was high the mean particle size appeared to stabilise (Figure 5b).

Mean estimates of SSC from the lower ADV (calculated later) were used to confirm that these spikes did not represent resuspension events (Figure 5d). In addition, this comparison showed that even though observations of SSC and d_{50} were strongly positively correlated at low values (below 20 mg L^{-1}), they showed no correlation at higher values.

5 Sediment calibration approach

Here we describe the two direct calibration methods, herein referred to as *in-situ* LISST method and *laboratory* OBS method. We then describe how indirect observations of SSC were connected together using the vertical profile of acoustic backscatter from the ADCP.

5.1 In-situ LISST method

The *in-situ* calibration method involved intensive ship-based vertical profiling near the lander mooring location (Figure 2ii). A LISST was fixed to the *RV Solander's* CTD rosette which profiled to collect co-located and concurrent LISST measurements and Niskin water bottle samples. The samples were collected across a range of depths. The profiling frame could not collect bottle samples closer than about 4 m ASB. This approach has been used previously for continental shelf and slope studies (e.g. Gardner et al., 1985; Puig et al., 2001).

We vacuum filtered water samples using 0.4 µm pre-weighed filter paper to determine SSC. Filtered samples were washed with deionised water and dried before weighing. The LISST sampled continuously at 1 Hz during profiling and, for each bottle sample, the closest two data points from the LISST were averaged to produce a corresponding point in the calibration data set. A total of 47 bottle samples were collected within 1,400 m of the lander.

5.2 Laboratory OBS method

The OBS instrument from the lander was calibrated post deployment in the laboratory. We used the sediment grab sample collected at the lander site to assess the instrument response in a recirculating tank, and our method followed SSC laboratory calibrations described previously by Downing and Beach (1989); Ludwig and Hanes (1990).

The key steps were:

1. water was recirculated in a 60 L tank to homogenise the sediment concentration;
2. OBS measurements (at 1 Hz) were taken in the tank, and a concurrent water sample was taken over a 30 second period;
3. the water sample was filtered using 0.4 µm pre-weighted filter paper;
4. more sediment was progressively added to increase SSC, and the process was repeated.

Water samples were processed as per the *in-situ* method. This process yielded 30 OBS data points per single SSC value.

5.3 Inference on acoustic backscatter

In the ocean environment, direct sampling adjacent to deployed instruments was not feasible. We overcame this by comparing data from the OBS, LISST, and both ADVs to the ADCP backscatter at the height of each instrument. The 1 MHz ADCP vertical profile was the key to inferring SSC at different heights because it gave us concurrent observations with every other instrument on the lander (in height ASB and time, Figure 3). Processed data from each of the deployed instruments could then be compared, e.g. OBS to ADCP, ADCP to ADV.

Each calibration model was assumed to be a linear model, based on theory and previous studies. Hence, inference of SSC for each ADV required propagation of raw ADV echo measurements through three linear models, plus a scale conversion: 1) ADV to ADCP

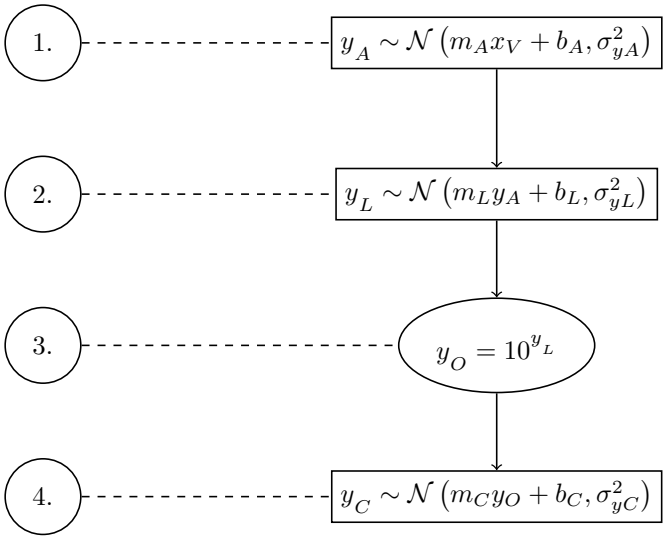

Figure 6. Directed acyclic graph of the connected models used to infer SSC for instruments where a direct calibration was not undertaken. The rectangular nodes are the linear models and the ellipse represents the conversion from the log_{10} decibel scale. Subscripts are as follows; V = ADV, A = ADCP, L = log_{10}(OBS), O = OBS, C = SSC. The LISST models could also be substituted for the OBS in steps 2 and 4 to predict SSC.

2) ADCP to OBS (or LISST) 3) conversion from log_{10} and 4) OBS (or LISST) to direct SSC (Figure 6). Once each calibration model was established, a single value from either ADV could be sampled n times through each model to give n estimates of SSC, the distribution of which contained the total uncertainty from the entire propagation process.

To produce the calibration data sets, 5-minute blocks (described previously) were averaged and the corrections and previously described flagging were applied. For each model, the corrected ADCP backscatter was then linearly interpolated to the height of the relevant instrument. The ADCP receivers saturated at elevated levels, resulting in a non-linear response compared to other instruments. This is a known limitation of the instrument (pers. comm. with Nortek Instruments). We removed saturated data from the analysis by applying an ADCP backscatter threshold value (82.5 dB pre-correction) determined by visual inspection to produce the four indirect calibration data sets.

6 Calibration results and discussion

6.1 In-situ LISST calibration

SSC from the filtered bottle samples ranged from 0.12–15.68 mg L^{-1} with a median and mean of 0.35 and 2.16 mg L^{-1}, respectively. A total of 47 data points collected between 4 and 55 m ASB were used for the linear least-squares fit (Figure 7c). Only 16 data points with SSC greater than 1.00 mg L^{-1} were collected from 47 bottles (Figure 8).

We used MCMC sampling (4 chains for 5,000 iterations with 2,000 tuning steps) to approximate the posterior probability distribution for the slope and intercept, m and b (Figure 7a), and the residual variance parameter, σ_y (Figure 7b). Priors were set with a mean of zero and a standard deviation of 10. The model results were stationary and ergodic (repeatable). This suggested that the posterior distributions were suitable for inference. Posterior predictive samples were drawn from the model for values from 0 to

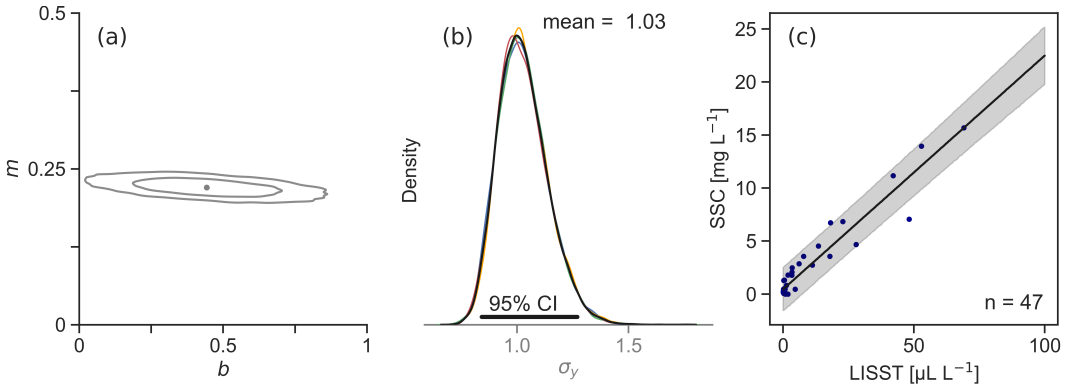

Figure 7. *In-situ* calibration results for the LISST: (a) sampling approximation to the posterior probability distribution for the model parameters, m and b, showing the mean with 68% and 95% highest probability density contours, (b) sampling approximation to the posterior probability distribution for the model residual term σ_y (mean in black, each chain coloured), and (c) data (dots) and mean outcome (line) with the 95% CI (grey shading).

100 µL L^{-1}, which allowed for estimation of the 95% posterior predictive CI (Figure 7c - grey shading).

The 95% CI were calculated for each model parameter (Table 2) and for estimates with a mean SSC value of 100 mg L^{-1} (Table 3). The posterior distribution was approximately normal and 95% CI remained relatively constant up to 5.0 (3.0, 7.0) mg L^{-1}. After this CI began to increase, reaching 20.0 (17.4, 22.6) mg L^{-1}, and up to 100.0 (90.9, 108.2) mg L^{-1}. This was driven by variability in the slope parameter owing to a lack of bottle samples at high SSC.

The weighted mean effective density for all samples, $\Delta\rho$, was represented by the slope, $m = 0.22$ (0.20, 0.24) (Figure 8c). This was similar to zero order aggregates observed by Krone (1986) and samples analysed by Mikkelsen and Pejrup (2001). This suggested, for higher concentration bottle samples at least, that the majority of the observed particles were flocs. The effective density was not constant, however, and appeared to be a function of particle size for samples over 1.00 mg L^{-1} (Figure 8a,b). Inclusion of mean particle size as an independent variable in the model did not have a significant effect on posterior predictive CI. Because of the low number of useful data points, and uncertainty on how well the bottle samples (collected at 4 m ASB and higher) represented conditions at the deployment height, it was decided not to include particle size in the model.

6.2 Laboratory OBS Calibration

The tank was filled with approximately 60 L of tap water and 19 water samples were taken as sediment from site was progressively added. Measured SSC ranged from 2.2–68.0 mg L^{-1}. OBS fluctuations in clear water (no sediment) with the pump running were less than ±1 NTU, but grew larger as SSC increased.

We calculated the model parameters in the same manner as the *in-situ* results (Table 2, Figure 9). MCMC sampling (4 chains for 5,000 iterations with 2,000 tuning steps) was used to approximate the posterior distribution for m and b (Figure 9a), and σ_y (Figure 9b). Posterior predictive samples of OBS data were drawn with a range of 0-70 NTU, which were used to calculate the 95% CI (Figure 9c - grey shading).

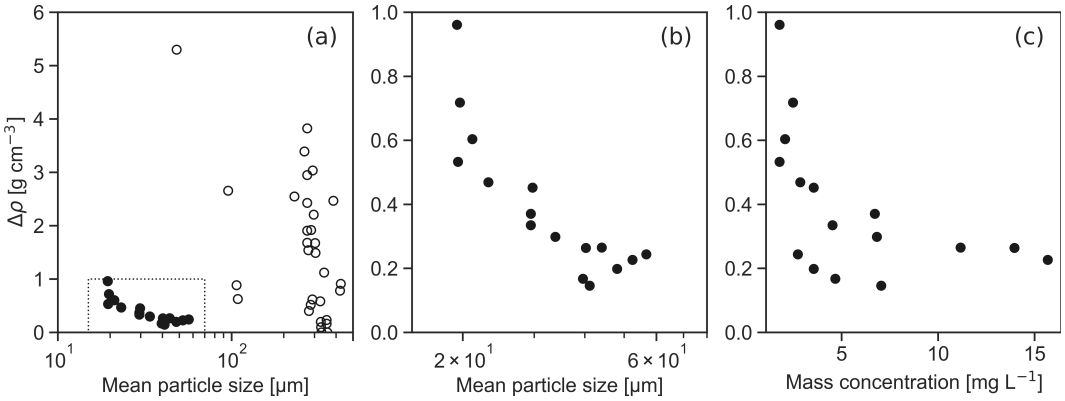

Figure 8. Calculated effective density, $\Delta\rho$, from in-situ data (a) for all samples (unfilled) and samples with SSC greater than 1.00 mg L^{-1} (filled), (b) inset of (a) (dashed box), and (c) against measured SSC.

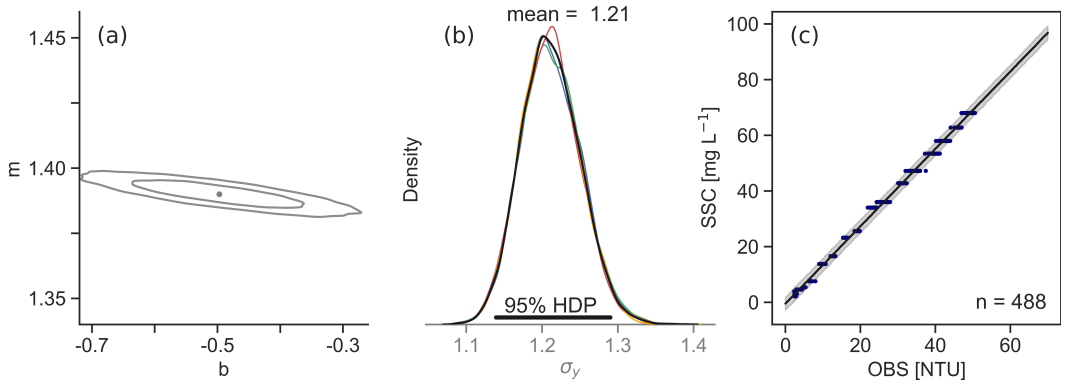

Figure 9. Laboratory calibration results for the OBS-SSC as per Figure 7.

Table 2. Bayesian linear model mean parameter estimates with the 95% CI shown in brackets

Model	b	m	σ_y
OBS - SSC (*laboratory*)	-0.497 (-0.669, -0.326)	1.39 (1.38, 1.40)	1.21 (1.140, 1.29)
LISST - SSC (*in-situ*)	0.438 (0.105, 0.772)	0.221 (0.201, 0.240)	1.03 (0.837, 1.27)
ADCP - OBS	-3.73 (-3.79, -3.67)	0.0559 (0.0551, 0.0567)	0.0916 (0.0885, 0.0948)
ADCP - LISST	-3.18 (-3.27, -3.08)	0.0622 (0.0609, 0.0634)	0.0882 (0.0849, 0.0916)
ADV 0.49 m - ADCP	30.6 (29.4, 31.9)	0.380 (0.369, 0.390)	0.521 (0.489, 0.555)
ADV 1.41 m - ADCP	30.8 (30.3, 31.3)	0.383 (0.379, 0.387)	1.18 (1.15, 1.21)

Posterior predictive CI remained relatively constant at approximately up to 100 (97.4, 102.4) mg L^{-1}. This was owing to our ability to control SSC in the laboratory and thus evaluate the instrument response at high concentrations. This resulted in significantly reduced uncertainty for predictions at 100 mg L^{-1} compared to the *in-situ* LISST calibration, despite having similar uncertainty for mean values under 20 mg L^{-1}.

The use of freshwater and an energetic pump were expected to limit flocculation, potentially increasing OBS response (per unit SSC). Conversely, fine sand particles with a faster settling rate, were probably not observed during profiling (note particles in this size class were observed by the LISST during profiling, but no analysis of filtered samples was performed to determine whether these were flocs or primary particles), were expected to remain suspended in the tank, potentially decreasing the OBS response (per unit SSC). Attempts to measure PSD in the tank were inconclusive, so the difference between *laboratory* and *in-situ* conditions was not able to be assessed.

6.3 Comparison of direct calibrations

We used field data to compare the *in-situ* and *laboratory* calibrations. Note that the OBS was located 0.27 m above the LISST. The 5-minute block-averaged data sets were converted to point estimates of SSC using the mean slope and intercept parameters from each model. Blocks where the current speed was less than 0.1 m s^{-1} were separated from the comparison as per the LISST flagging.

The calculated SSC from the OBS and LISST field data sets compared well for the bulk of the data (Figure 10), although scatter increased with SSC. The maximum *a posteriori* slope calculated by linear least-squares fitting of the data sets was 1.08 (Figure 10 - right), which indicated that the OBS estimated SSC 8% higher than the LISST on average, despite being moored 0.27 m above it. During the propagation of NLIW (i.e. at maximum SSC) the OBS produced estimates 20 to 30% higher than the LISST.

6.4 Extension to acoustic instruments

We developed four calibration models utilizing the ADCP backscatter measurements: ADCP-OBS, ADCP-LISST, ADV141-ADCP, and ADV049-ADCP (the latter two are the ADVs at 1.41 m and 0.49 m). Blocks where the current speed was less than 0.1 m s^{-1} were not used in any model. The models were developed in the same manner as the in-situ and laboratory models (Figure 11, Table 2). The standard deviation of the prior for the intercept was increased to 50 for the ADV models. The rate of good data return from the ADCP increased with height ASB.

The y-residuals for each model were plotted against mean diameter measurements from the LISST to investigate the influence of particle size variation (not shown). Only the ADV141-ADCP model showed any trend, which suggested that residual variance was

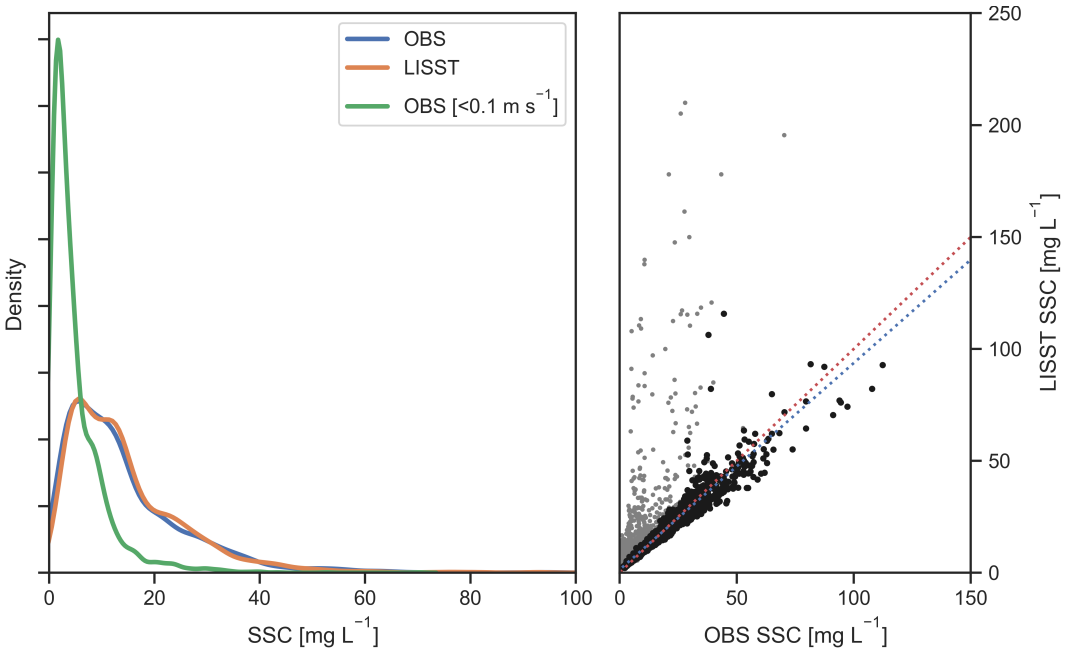

Figure 10. (left) histograms of SSC estimates for the entire field deployment from the OBS and LISST calibration models; and (right) a comparison of the OBS and LISST SSC estimates (black dots), with data points where current speed was less than 0.1 m s^{-1} identified (light grey), and the 1:1 line (dotted red) and maximum *a posteriori* least-squares fit (dotted blue).

dominated by measurement noise for the other three models, despite the theoretical dependence of each instrument on particle size (note the significant bad data return from the ADCP due to saturation, especially for the ADV049-ADCP model). The residual-particle size trend for the ADV141 model was non-linear, potentially a function of the different scattering and viscous attenuation for each frequency as particle size changes. Given that the complex acoustic response of cohesive sediment was beyond the scope of this work, and given the incomplete data from the ADCP due to saturation, this trend was not included in the model directly, but rather captured as increased variance in the residual parameter, σ_y (Table 2).

Inference of SSC from the ADCP and each ADV was possible via either the LISST or OBS models. For example, n samples from an ADV-ADCP model could be passed into the ADCP-LISST model and transformed into n different log_{10}(LISST) estimates. Finally they could then be transformed out of log_{10} space and passed into the LISST-SSC model to produce n estimates of SSC for a single ADV measurement (Figure 6). The same process could be done with the ADCP-OBS and OBS-SSC models, producing a different set of n SSC estimates. When posterior predictive samples are drawn from a model there is growth in uncertainty. The 95% CI from any one model sampling was less than ±10%. Transformation from log_{10} space, however, whilst not adding any additional uncertainty itself, increased the variance (about the distribution mean) and skewed the sample distribution (Figure 12 - step 3). This step was unavoidable as the acoustic instruments native measurements were on the decibel scale.

For a given mean SSC value of 100 mg L^{-1}, the SSC 95% CI were calculated for each instrument and pathway (Table 3). There was a marked difference between the CI for the different instruments and models. For the previous ADV sample propagation example, the width of the 95% CI (about the mean) increased from 0% to 7.8% at step 1,

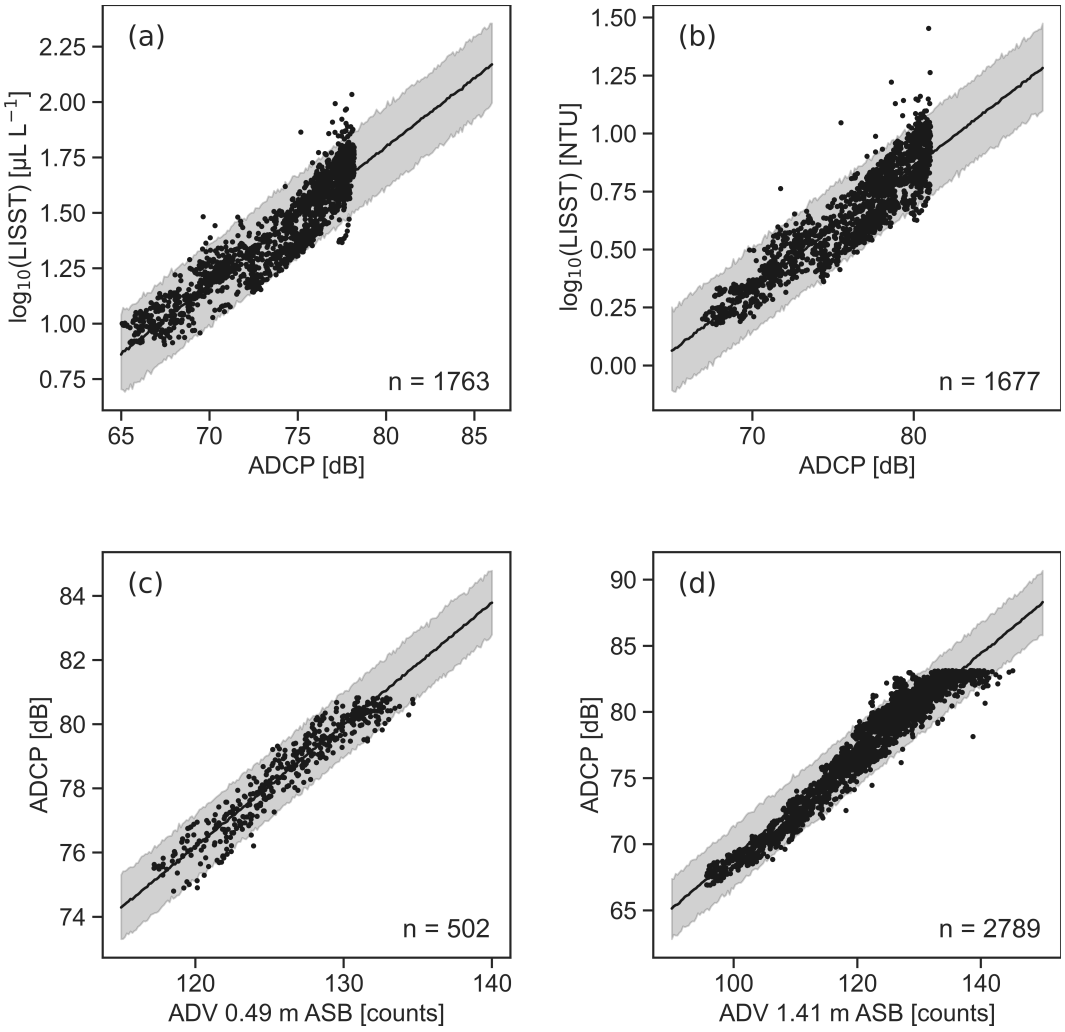

Figure 11. Data (dots) and mean regression outcome (line) with the 95% CI posterior predictive intervals (grey shading) from model sampling for the ADCP linear model with (a) the LISST, (b) the OBS, (c) the lower ADV, and (d) the upper ADV.

Table 3. Upper and lower 95% credible interval SSC estimates for each instrument and pathway (where applicable), based on predictions at a mean value of 100 mg L^{-1}.

Model	SSC 95% CI (mean of 100 mg L^{-1})
OBS	97.4, 102.4
LISST	90.9, 108.2
ADCP (via OBS)	58.3, 160.5
ADCP (via LISST)	52.6, 173.8
ADV 0.49 m (via OBS)	56.2, 165.0
ADV 0.49 m (via LISST)	50.8, 176.4
ADV 1.41 m (via OBS)	54.0, 167.3
ADV 1.41 m (via LISST)	50.9, 177.8

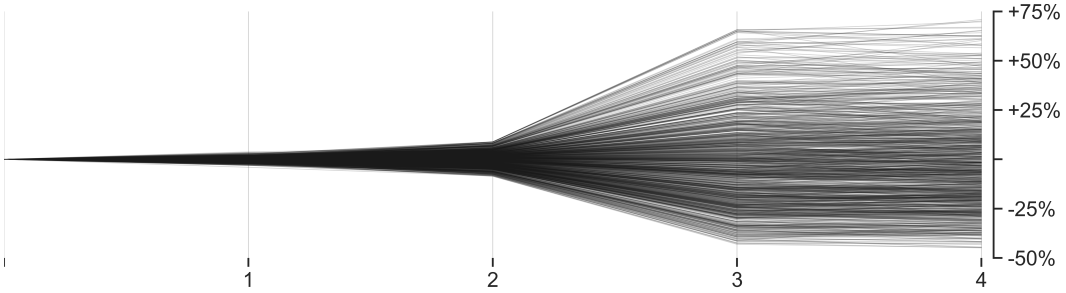

Figure 12. Propagation of a single backscatter value from ADV 1.41 m ASB sampled 1,000 times through the four transformations shown in Figure 6 using the LISST models. Lines represent the 95% highest probability results of the 1,000 samples.

to 17.5% at step 2, to 109% at step 3, and to 116% at step 4 (Figure 12). Using the OBS pathway only reduced the final CI width by about 4%. Given the LISST was sensitive to flocculation, all estimates of SSC from the acoustic instruments presented hereafter used the OBS calibration pathway, unless stated otherwise.

7 Sediment dynamics influenced by NLIW passage

Using the calibration models it was now straightforward to convert time series of raw data (such as ADV echo intensity) to estimates of SSC with uncertainty. A time series of 20,000 SSC sample estimates was generated using the boxcar-filtered data for each instrument. From these samples the mean outcome and CI were then calculated. Several other quantities were also able to be derived.

Estimates of mean SSC were calculated for the ADCP, OBS, and each ADV for the first 15 full days of the deployment (Figure 13). Estimates of uncertainty are shown in later figures as they were difficult to observe at this time scale. Temperature data from the nearest TWC mooring and mean horizontal current speed at the 0.49 m ASB ADV give context to the observations (Figure 13a,b). Current speed measurements were converted to bed shear stress estimates τ_{bed}, using the quadratic drag law with $C_d = 0.00185$ (Zulberti et al., 2018).

SSC peaks were positively correlated with bed stress in both time and magnitude. SSC at the lower ADV repeatedly increased to around 100 mg L^{-1} when τ_{bed} reached 0.4 N m^{-2}, and always showed some response when τ_{bed} exceeded 0.07 N m^{-2} for a 5-minute block (roughly 0.2 m s^{-1}). SSC from the ADCP showed intermittent bursts of

elevated SSC (over 5 mg L^{-1}), occasionally reaching more than 20 m above the bed throughout both spring tidal cycles (Figure 13c). Interference from reflections off instruments on the lander T-string were also observed in the ADCP record (small dark brown patches in Figure 13c).

Current speed and mean SSC from the lower ADV (0.49 m ASB) were used to estimate the horizontal sediment flux, or transport (at this elevation). Each NLIW (near the start of the deployment) generated strong near-bed currents in the off-shelf direction that drove a significant short-term asymmetric SSC flux (not shown). This flux time series was used to calculate the wavelet power spectrum (Figure 13e), demonstrating the ability the short-period NLIW to drive enhanced horizontal sediment fluxes, which subsequently enhanced the transport capacity of longer time-scale motions (around half the M2 tidal frequency). In general, mean SSC was about twice as high during the first spring tidal cycle when the NLIW were largest and, as a result, the flux at tidal timescales was significantly greater.

The two largest NLIW occurred near the beginning of the deployment around 12 hours apart (Figure 14a), denoted Wave 1 and Wave 2. Both waves were composed of a well-defined initial depression with amplitudes of about 60 and 70 m, respectively. The well-defined waves were followed by a series of smaller oscillations. The NLIW-induced currents were superimposed on barotropic and linear baroclinic motions (Figure 14b). We used the high resolution 8 Hz ADCP backscatter to calculate the mean SSC over the bottom 23 m. The mixing layer pycnocline (MLP) dynamics were analysed in detail by Zulberti et al. (2020), who demonstrated that the sharp drop in ADCP backscatter was a suitable proxy for the MLP position.

Mean and 95% CI of SSC were calculated for each ADV, the OBS, and the LISST (Figure 14d). SSC estimates from the LISST were highly sensitive to flocculation and thus showed significant deviations from the other instruments when the current speed was less than 0.1 m s^{-1}. These deviations were always accompanied by significant spikes in mean particle size (Figure 14e) and beam attenuation (not shown). The size of these spikes was weakly positively correlated with the length of time the currents remained low and the SSC prior to each quiescent period. This resulted in LISST and beam attenuation spikes that were not correlated with current speed (or bed stress). This process of rapid floc growth during calm periods may be another cause of uncorrelated beam attenuation spikes worth considering in fine-grained marine environments, in addition to previously suggested causes, such as vertical velocities resulting from global instabilities (Bogucki et al., 1997); and trawling activities (Churchill et al., 1988).

Despite SSC falling by almost a half within about 20-30 minutes of each peak, elevated SSC was maintained for 5 to 6 hours after the wave passage. This was likely because of slow settling flocs that continued to be advected horizontally and vertically by the internal tide. After Wave 1, particles appeared to be vertically advected up to 50 m ASB by baroclinic motion, as observed by LISST and bottle sample measurements during a profile at approximately day 92.15 (not shown).

More detail in SSC and its uncertainty is evident when we focus on the NLIW events (Figure 15 and Figure 16). During Wave 1 the bed stress peaked at approximately 1 N m^{-2} under the wave trough. Cross-correlation of phase-lagged current speed and SSC signals suggested that sediment concentration lagged current speed by approximately 6 and 13 minutes at 0.49 and 1.41 m ASB, although the peak values only lagged by 0 and 5 minutes, respectively.

The peak estimates of SSC during Wave 1 were 150 (93.7, 233) mg L^{-1} at the lower ADV, 78.8 (47.1, 125) mg L^{-1} at the upper ADV, and 102 (93.2, 112) mg L^{-1} for the LISST. There was incomplete data return for the OBS during Wave 1 when turbidity exceeded the instrument limit. Elevated SSC was confined close to the bed until the ini-

tial wave trough passed and an upward vertical velocity (not shown) was measured by the ADCP (Figure 15c).

Wave 2 exhibited similar peak magnitudes of current speed and SSC, although the average current speed was higher than during Wave 1 (Figure 16). SSC estimates peaked at 161 (101, 246) mg L^{-1} at the lower ADV, 79.0 (46.9, 129) mg L^{-1} at the upper ADV, 108 (106, 110) mg L^{-1} for the OBS, and 82.4 (75.0, 90.0) mg L^{-1} for the LISST. The wave form was less coherent and vertical resuspension was confined closer to the bed. SSC signal lagged current speed by approximately 4 and 9 minutes at 0.49 and 1.41 m ASB, and the peak values lagged by 3 and 7 minutes, respectively.

Using the full distribution of SSC estimates we derived three quantities of interest: the height of constant SSC (Figure 17a); the vertical gradient of SSC between each ADV (Figure 17b); and the time-rate-of-change at the lower ADV (Figure 17c). We used the boxcar-filtered ADCP-derived SSC data to calculate the 10 mg L^{-1} isopleth mean and 95% CI (Figure 17a). The vertical gradient of SSC, dC/dz, exhibited large uncertainty, with CI difference up to 170 mg L^{-1} m^{-1}, and could be negative. This will have consequences for the estimation of the vertical turbulent flux and is the subject of future research. The time-rate-of-change of SSC, dC/dt, was more uncertain during periods of large gradients and showed small uncertainty when the gradient was near zero.

Vertical profiles of SSC can be used to infer sediment resuspension and deposition. For example, during Wave 1, near-bed SSC was strongly positively correlated with current speed (Figure 15c,d). In contrast, the ADCP data demonstrated that measurements of SSC between 6 and 12 m ASB were negatively correlated with current speed. This highlights the inherent hysteresis of the process and the potential for experimental design to influence the final interpretation, especially when limited instrumentation is available close to the sea bed (e.g. Bogucki et al., 1997). A more detailed examination of the vertical resuspension and deposition processes is a key focus for future work using this data set.

We also observed good agreement between the vertical displacement of isotherms and SSC from the ADCP, especially during Wave 1 (Figure 15a,c). This is in contrast to observations from Quaresma et al. (2007), who showed backscatter opposing isotherm movement.

Finally, we were able to observe the effect of PSD changes on SSC estimates via the LISST during Wave 1 (Figure 15d,e). Whilst not as significant as the spikes observed during calm periods, measurements from the LISST showed a negative correlation with current speed between 0.05 and 0.4 m s^{-1}. During Wave 2 (and the peak of Wave 1), when current speed was consistently greater than 0.4 m s^{-1}, the observed PSD was relatively constant. This is in agreement with the LISST flagging observations (Figure 5). In addition, this process of floc aggregation and breakup appeared to respond almost instantly to changes in current speed, i.e. the process had virtually no time memory.

8 Conclusions and recommendations

We used Bayesian inference to estimate SSC from a suite of lander instruments, with a full description of model uncertainty. This calibration method made it straightforward to derive meaningful statements about the potential range of SSC from native instrument observations.

To our knowledge, this was the first attempt to calibrate bottom-lander based instruments on the continental shelf using in-situ SSC measurements. The comparison to a traditional laboratory calibration appeared to be favourable, although several limitations in both methods reduced our confidence in the final results. Firstly, because of the sporadic nature and large changes in SSC that occurred during the resuspension events

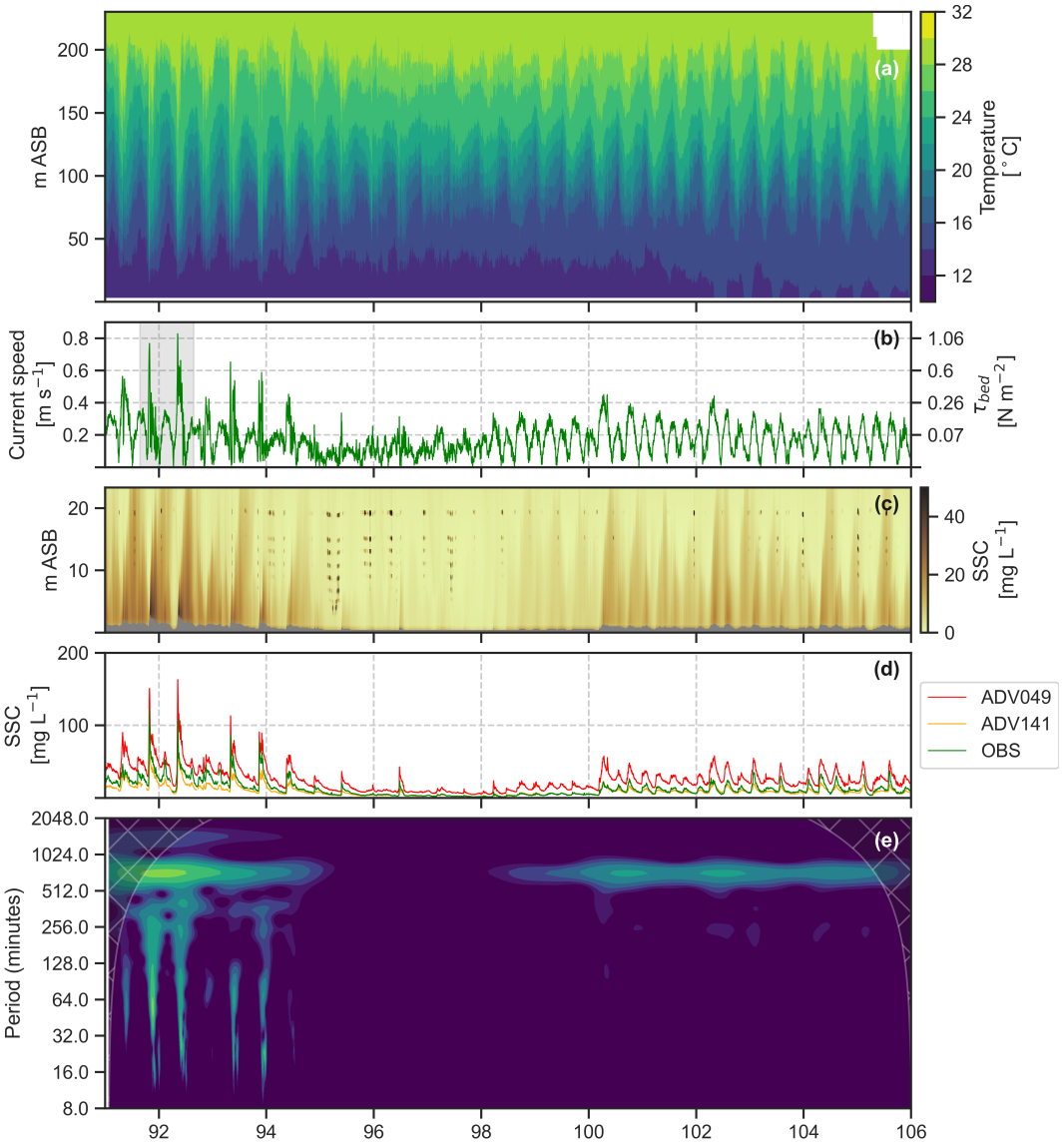

Figure 13. KISSME 2017 deployment data; (a) TWC temperature from SP250, (b) boxcar-filtered current speed measured at 0.49 m ASB (with conversion to bed stress on the right y-axis), (c) calibrated ADCP backscatter with grey areas indicating receiver saturation, (d) mean estimates of SSC, and (e) the wavelet power spectrum of cross-shelf sediment flux at 0.49 m ASB using the ADV current speed and mean SSC estimate. The grey shading in (b) indicates the bounds of Figure 14. The x-axis shows days in 2017.

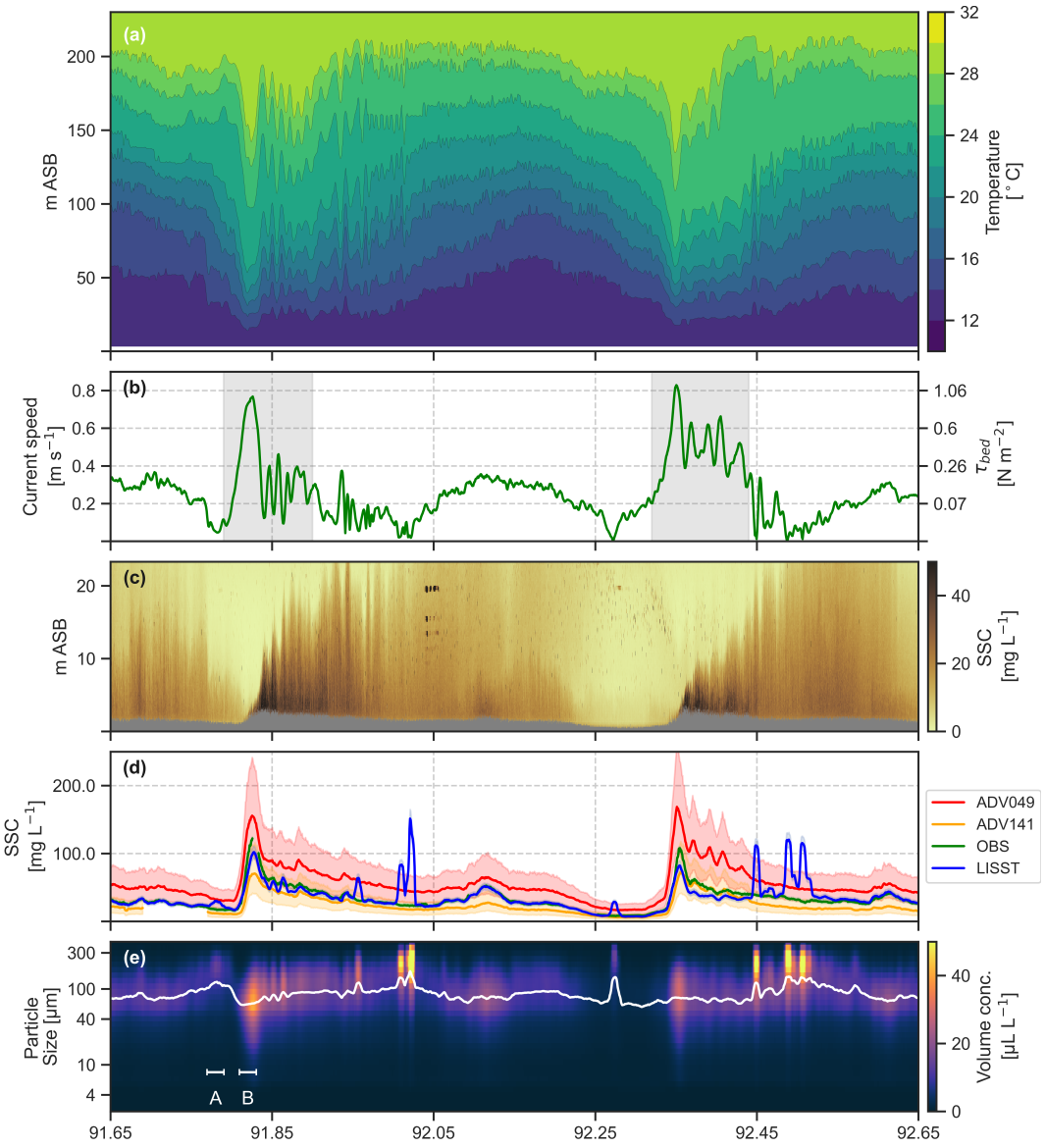

Figure 14. A 24-hour period presented as per 13 with the following changes; (d) SSC estimates now include the LISST and all 95% CI, shown as shading, with data points where current speed is less than 0.1 m s^{-1} included to show the effect on LISST measurements, (e) the boxcar-filtered (5-minute mean) LISST binned volume concentration data with the mean diameter (white line). grey shading on (c) indicates the bounds of Figure 15 and Figure 16. The labels A and B on (e) indicate the averaging period for the PSD shown in Appendix A. The x-axis shows days in 2017.

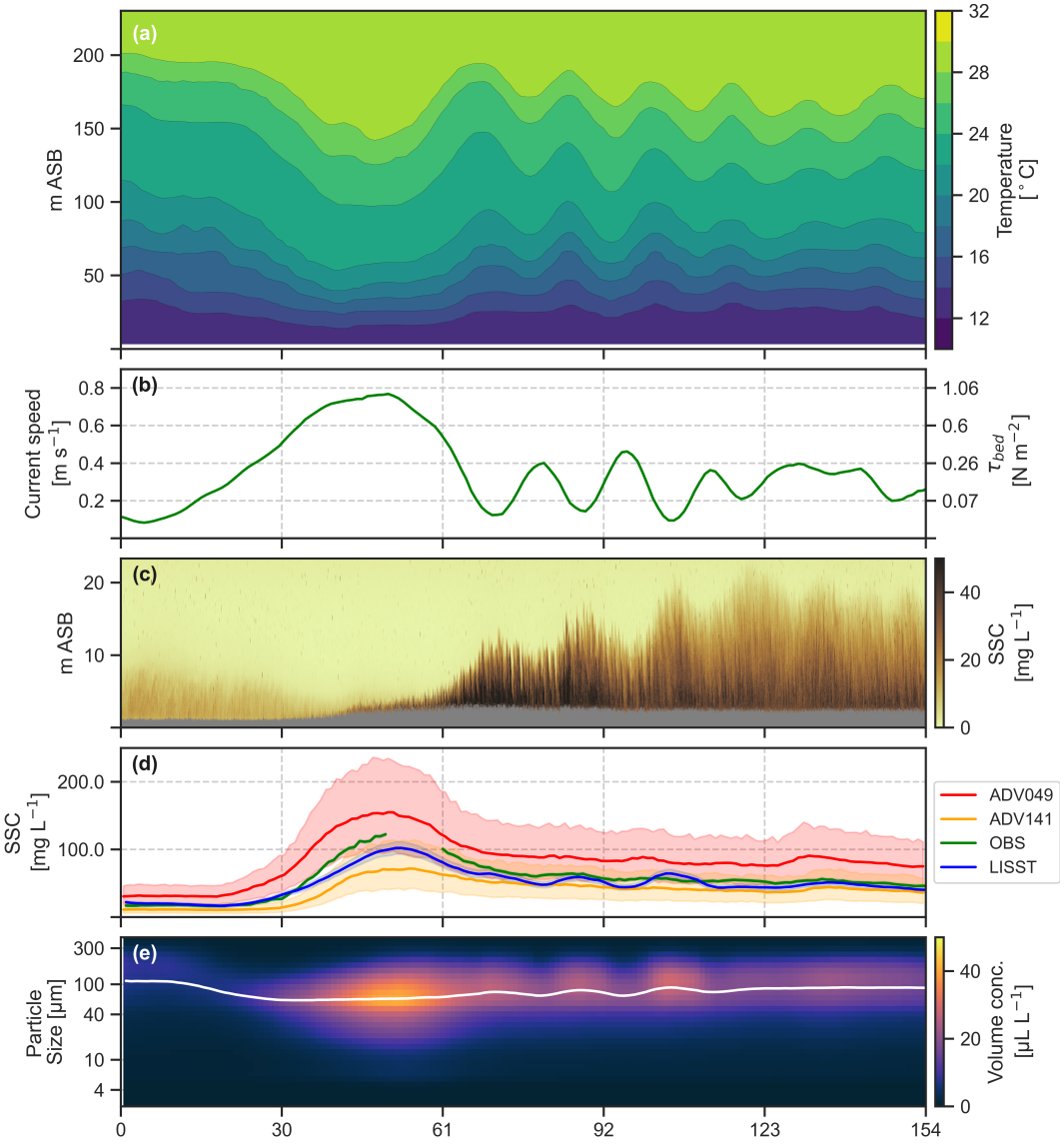

Figure 15. Wave 1 displayed as per Figure 14. The x-axis shows minutes.

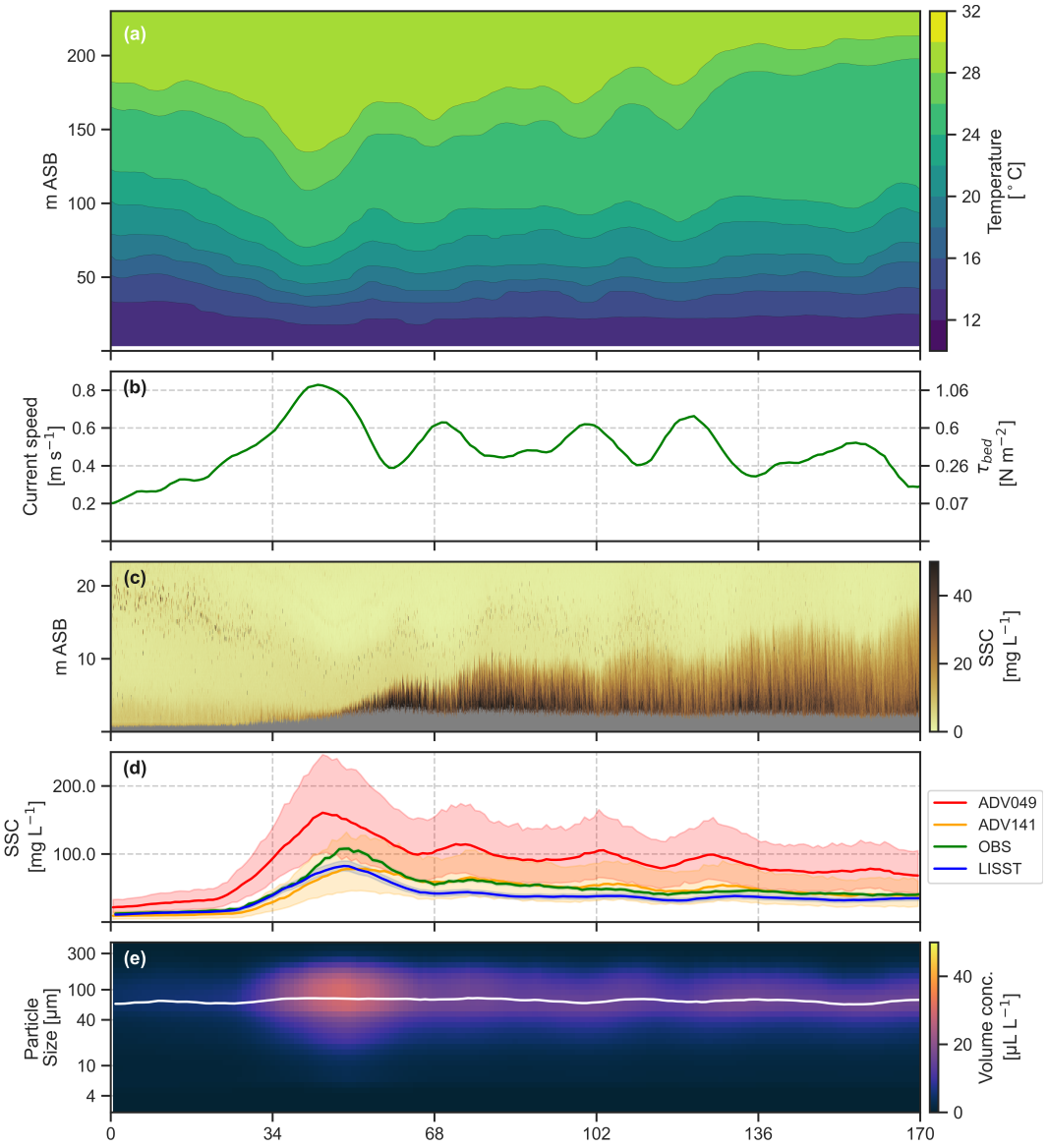

Figure 16. Wave 2 displayed as per Figure 14. The x-axis shows minutes.

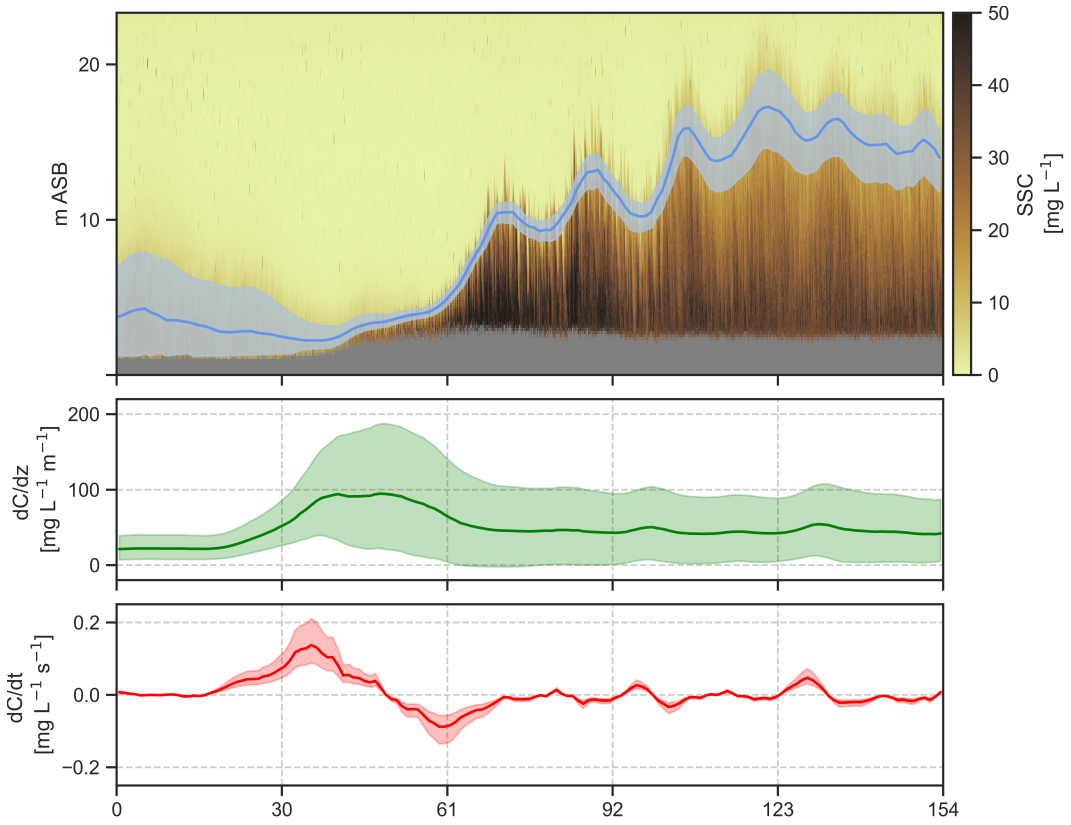

Figure 17. Derived quantities with uncertainty; (a) the 10 mg L^{-1} isopleth showing the mean (line) and 95% CI (blue shading) calculated using the boxcar-filtered data and shown over the high resolution ADCP SSC mean estimate; (b) the vertical gradient of SSC between each ADV with 95% CI; and (c) the time-rate-of-change at the lower ADV (0.49 m ASB). The x-axis shows minutes.

at our site, it proved difficult to collect bottle samples that were representative of the deployment observations. Peak SSC estimates from the lander deployment were occasionally an order of magnitude larger than the highest SSC bottle sample collected, although this uncertainty was able to be captured by the model (assuming the linear relationship held).

Second, our *in-situ* profiling calibration strategy may have missed the presence of a near-bed layer with different PSD properties to the particles in suspension further from the bed. Due to the profiler design and setup we were unable to collect bottle samples within 4 m of the bed. Zulberti et al. (2020) found that the log-layer was typically less than 1 m for the experiment. Comparison of profiling data with the lander-based LISST as it was lowered to the sea floor indicated a distinct increase in the measured d_{50} near the bed (not shown). This was likely because of the presence of larger primary particles with a higher settling velocity that were generally only located close to the bed (e.g. Agrawal & Hanes, 2015). If true, this would suggest that $\Delta\rho$ (and hence the in-situ LISST-SSC calibration slope) may be higher close to the bed, resulting in an underestimate of SSC.

Third, the laboratory calibration did not replicate field conditions, namely the salinity, temperature, and turbulence intensity levels were not re-created and as a result it is unlikely the suspended PSD in the laboratory was similar to the ocean BBL. Primary particles with diameters less than 4 μm were never observed disaggregated in-situ, whereas in the laboratory the presence of these particles may have increased OBS response per unit SSC, resulting in an underestimate of SSC.

In order to improve confidence in future efforts we have summarised four key recommendations for near-bed deep water SSC calibration based on the lessons learned from this work.

1. Be skeptical of laboratory calibrations (that do not mimic in-situ conditions) when cohesive sediment is present.
2. Ideally any (or every) instrument used for SSC analysis should be calibrated in-situ, i.e. attach OBS and ADV instruments to the profiling frame. Vertical co-location of a calibrated OBS and ADV on a bottom-lander frame should reduce uncertainty when only the OBS can be calibrated in-situ.
3. In-situ calibration should aim to sample from the same height as the original deployment, if possible. Frame adjustments should be considered if necessary.
4. Due to their apparent sensitivity to flocculation, laser scattering and beam attenuation measurements should always be compared to other instrument types (if possible) when cohesive sediment is present.

Nevertheless, we were able to calibrate the suite of lander-based instruments and derive estimates of uncertainty for field observations of SSC under large amplitude NLIW. We confirmed that sediment is restricted to the near-bed mixing layer during the passage of internal waves (as per Zulberti et al., 2020), and showed that a strong vertical gradient of SSC still exists within this layer, albeit with significant uncertainty. Using the full profile of ADCP backscatter we were able to predict the evolution of an SSC isopleth and the inherent lag in SSC at different heights above the bed. Detailed quantitative analysis, utilising the probabilistic objects presented here, is the focus of ongoing research.

Appendix A Sea bed sediment grab sample

A sediment sample was collected from the sea bed using a Smith McIntyre grab. The sample was collected over the lander location after the mooring was recovered. A portion of the sample, collected from the top, was used to determine the PSD through a combination of sieving and laser diffraction (Figure A1). A laboratory particle size anal-

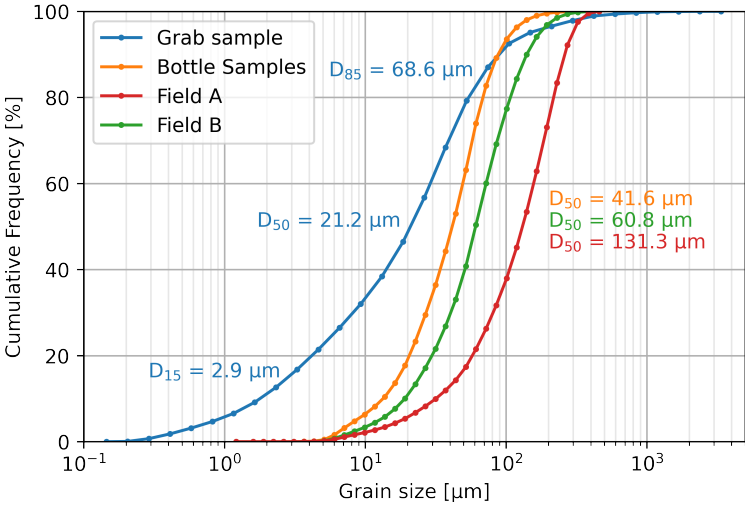

Figure A1. Cumulative particle size distributions from the grab sample (analysed in the laboratory; blue line), LISST measurements for profiling Niskin bottle samples (weighted mean; orange line), and two 30 minute periods from the deployment (indicated on Figure 14(e); green and red lines). Field A represents relatively quiescent conditions and Field B represents energetic conditions (high SSC and floc breakup). Plotted points indicate the geometric mean of each bin.

yser measured the size distribution at $\phi 0.5$ ($\phi = -2log_2(D)$ where D is the particle diameter in mm) and utilised a sonication probe to disperse aggregates.

The median grain size was 21.2 µm with around 20% fines (<3.9 µm) and 18% (mostly fine) sand (>63 µm) as per the Wentworth grain size classification. Despite this, the LISST never measured particles smaller than around 4 µm in-situ, suggesting that flocculation was an important process at this site. A comparison between the PSD of the weighted-average bottle samples and two 30 minute periods from the deployment (Figure 14) underscored the potential variation in PSD both spatially and temporally (Figure A1).

Acknowledgments

We thank Andrew Zulberti for the provision of processed ADV and ADCP data used in this work. We thank Andrew Zulberti, Yankun Gong, and Connor Duffin for their discussions on these experiments that have aided in the analysis techniques and interpretation of these observations. We thank the staff of AIMS, crew of the R. V. Solander, and other UWA staff and students for their assistance with the fieldwork. This work was funded by the Australian Research Council (ARC) Research Training Program scholarship, the ARC Industrial Transformation Research Hub for Offshore Floating Facilities (IH140100012), and an ARC Discovery Grant (DP140101322).

Through-water-column mooring data from this experiment are archived on the UWA library research data repository (https://doi.org/10.4225/23/5afbf8fc55ed1). Bottom lander ADV and ADCP data used in this manuscript are archived on the UWA library research data repository (https://doi.org/10.26182/5f62f6e361872). Optical backscatter, LISST, sediment grab, and water sampling data used in this manuscript are archived on the UWA library research data repository (https://doi.org/10.26182/hyw0-my35).

References

Agrawal, Y. C., & Hanes, D. M. (2015). The implications of laser-diffraction measurements of sediment size distributions in a river to the potential use of acoustic backscatter for sediment measurements. *Water Resources Research*, *51*(11), 8854–8867. doi: 10.1002/2015WR017268

Boegman, L., & Stastna, M. (2019). Sediment Resuspension and Transport by Internal Solitary Waves. *Annual Review of Fluid Mechanics*, *51*(1), annurev–fluid–122316–045049. doi: 10.1146/annurev-fluid-122316-045049

Bogucki, D., Dickey, T., & Redekopp, L. G. (1997). Sediment resuspension and mixing by resonantly generated internal solitary waves. *Journal of Physical Oceanography*, *27*(7), 1181–1196. doi: https://doi.org/10.1175/1520-0485(1997)027⟨1181:SRAMBR⟩2.0.CO;2

Bonnin, J., Van Haren, H., Hosegood, P., & Brummer, G. J. A. (2006). Burst resuspension of seabed material at the foot of the continental slope in the Rockall Channel. *Marine Geology*, *226*(3-4), 167–184. doi: 10.1016/j.margeo.2005.11.006

Butman, B., Alexander, P. S., Scotti, A., Beardsley, R. C., & Anderson, S. P. (2006). Large internal waves in Massachusetts Bay transport sediments offshore. *Continental Shelf Research*, *26*(17-18), 2029–2049. doi: 10.1016/j.csr.2006.07.022

Cacchione, D. A., & Drake, D. E. (1986). Nepheloid layers and internal waves over continental shelves and slopes. *Geo-Marine Letters*, *6*(3), 147–152. doi: 10.1007/BF02238085

Cacchione, D. A., Pratson, L. F., Ogston, A. S., Pratson, L. F., & Ogston, A. S. (2002). The shaping of continental slope by internal tides. *Science*, *296*(April), 724. doi: 10.1126/science.1069803

Cheriton, O. M., McPhee-Shaw, E. E., Shaw, W. J., Stanton, T. P., Bellingham, J. G., & Storlazzi, C. D. (2014). Suspended particulate layers and internal waves over the southern Monterey Bay continental shelf: An important control on shelf mud belts? *Journal of Geophysical Research: Oceans*, *119*(1), 428–444. doi: 10.1002/2013JC009360

Churchill, J. H., Biscaye, P. E., & Aikman, F. (1988). The character and motion of suspended particulate matter over the shelf edge and upper slope off Cape Cod. *Continental Shelf Research*, *8*(5-7), 789–809. doi: 10.1016/0278-4343(88)90077-5

Downing, J. P., & Beach, R. A. (1989). Laboratory apparatus for calibrating optical suspended solids sensors. *Marine Geology*, *86*(2-3), 243–249. doi: 10.1016/0025-3227(89)90053-4

Fugate, D. C., & Friedrichs, C. T. (2002). Determining concentration and fall velocity of estuarine particle populations using adv, obs and lisst. *Continental Shelf Research*, *22*(11-13), 1867–1886. doi: 10.1016/S0278-4343(02)00043-2

Gardner, W. D. (1989). Periodic resuspension in Baltimore Canyon by focusing of internal waves. *Journal of Geophysical Research*, *94*(C12). doi: 10.1029/jc094ic12p18185

Gardner, W. D., Biscaye, P. E., Zaneveld, J. R., & Richardson, M. J. O. (1985). Calibration and comparison of the LDGO Nephelometer and the OSU Transmissometer on the Nova Scotian Rise. *Marine Geology*, *66*, 323–344. doi: 10.1016/0025-3227(85)90037-4

Gartner, J. W. (2004). Estimating suspended solids concentrations from backscatter intensity measured by acoustic Doppler current profiler in San Francisco Bay, California. *Marine Geology*, *211*(3-4), 169–187. doi: 10.1016/j.margeo.2004.07.001

Gelman, A., Carlin, J., Stern, H., Dunson, D., Vehtari, A., & Rubin, D. (2013). *Bayesian data analysis* (3rd ed.). CRC Press.

Gibbs, R. J., & Wolanski, E. (1992). The effect of flocs on optical backscattering

measurements of suspended material concentration. *Marine Geology*, *107*(4), 289–291. doi: 10.1016/0025-3227(92)90078-V

Green, M. O., & Boon, J. D. (1993). The measurement of constituent concentrations in nonhomogeneous sediment suspensions using optical backscatter sensors. *Marine Geology*, *110*(1-2), 73–81. doi: 10.1016/0025-3227(93)90106-6

Ha, H., Hsu, W.-Y., Maa, J.-Y., Shao, Y., & Holland, C. (2009). Using ADV backscatter strength for measuring suspended cohesive sediment concentration. *Continental Shelf Research*, *29*(10), 1310–1316. doi: 10.1016/J.CSR.2009.03.001

Hoitink, A., & Hoekstra, P. (2005). Observations of suspended sediment from ADCP and OBS measurements in a mud-dominated environment. *Coastal Engineering*, *52*(2), 103–118. doi: 10.1016/J.COASTALENG.2004.09.005

Hosegood, P., Bonnin, J., & van Haren, H. (2004). Solibore-induced sediment resuspension in the Faeroe-Shetland channel. *Geophysical Research Letters*, *31*(9), 2–5. doi: 10.1029/2004GL019544

Jones, N. L., Ivey, G. N., Rayson, M. D., & Kelly, S. M. (2020). Mixing Driven by Breaking Nonlinear Internal Waves. *Geophysical Research Letters*, *47*(19). doi: 10.1029/2020GL089591

Klymak, J. M., & Moum, J. N. (2003). Internal solitary waves of elevation advancing on a shoaling shelf. *Geophysical Research Letters*, *30*(20). doi: 10.1029/2003GL017706

Krone, R. B. (1986). The significance of aggregate properties to the transport process. *Estuarine Cohesive Sediment Dynamics: Proceedings of a Workshop on Cohesive Sediment Dynamics with Special Reference to Physical Processes in Estuaries, Tampa, Florida, November 12–14, 1984*, 66–84. doi: 10.1007/978-1-4612-4936-8

Ludwig, K. A., & Hanes, D. M. (1990). A laboratory evaluation of optical backscatterance suspended solids sensors exposed to sand-mud mixtures. *Marine Geology*, *94*(1-2), 173–179. doi: 10.1016/0025-3227(90)90111-V

MacDonald, I. T., Vincent, C. E., Thorne, P. D., & Moate, B. D. (2013). Acoustic scattering from a suspension of flocculated sediments. *Journal of Geophysical Research: Oceans*, *118*(5), 2581–2594. doi: 10.1002/jgrc.20197

Manderson, A., Rayson, M. D., Cripps, E., Girolami, M., Gosling, J. P., Hodkiewicz, M., ... Jones, N. L. (2019). Uncertainty quantification of density and stratification estimates with implications for predicting ocean dynamics. *Journal of Atmospheric and Oceanic Technology*, *36*(8), 1313–1330. doi: 10.1175/JTECH-D-18-0200.1

McPhee-Shaw, E. E., Sternberg, R. W., Mullenbach, B., & Ogston, A. S. (2004). Observations of intermediate nepheloid layers on the northern California continental margin. *Continental Shelf Research*, *24*(6), 693–720. doi: 10.1016/j.csr.2004.01.004

Mikkelsen, O. A., Hill, P. S., Milligan, T. G., & Chant, R. J. (2005). In situ particle size distributions and volume concentrations from a LISST-100 laser particle sizer and a digital floc camera. *Continental Shelf Research*, *25*(16), 1959–1978. doi: 10.1016/J.CSR.2005.07.001

Mikkelsen, O. A., & Pejrup, M. (2001). The use of a LISST-100 laser particle sizer for in-situ estimates of floc size, density and settling velocity. *Geo-Marine Letters*, *20*(4), 187–195. doi: 10.1007/s003670100064

Moum, J. N., Caldwell, D. R., Nash, J. D., & Gunderson, G. D. (2002). Observations of Boundary Mixing over the Continental Slope. *Journal of Physical Oceanography*, *32*(7), 2113–2130. doi: 10.1175/1520-0485(2002)032⟨2113:OOBMOT⟩2.0.CO;2

Noble, M. A., & Xu, J. P. (2003). Observations of large-amplitude cross-shore internal bores near the shelf break, Santa Monica Bay, CA. *Marine Environmental Research*, *56*(1-2), 127–149. doi: 10.1016/S0141-1136(02)00328-8

Puig, P., Palanques, A., & Guillén, J. (2001). Near-bottom suspended sediment variability caused by storms and near-inertial internal waves on the Ebro mid continental shelf (NW Mediterranean). *Marine Geology*, *178*(1-4), 81–93. doi: 10.1016/S0025-3227(01)00186-4

Quaresma, L. S., J., V., Oliveira A., J., S., Vitorino, J., Oliveira, A., & da Silva, J. (2007). Evidence of sediment resuspension by nonlinear internal waves on the western Portuguese mid-shelf. *Marine Geology*, *246*(2-4), 21. doi: 10.1016/j.margeo.2007.04.019

Rayson, M. D., Jones, N. L., & Ivey, G. N. (2019). Observations of Large-Amplitude Mode-2 Nonlinear Internal Waves on the Australian North West Shelf. *Journal of Physical Oceanography*, *49*(January 2019), 309–329. doi: 10.1175/JPO-D-18-0097.1

Salvatier, J., Wiecki, T. V., & Fonnesbeck, C. (2016). Probabilistic programming in Python using PyMC3. *PeerJ Computer Science*, *2016*(4), 1–24. doi: 10.7717/peerj-cs.55

Sandstrom, H., & Elliott, J. A. (1984). Internal Tide and Solitons on the Scotian Shelf: a Nutrient Pump At Work. *Journal of Geophysical Research*, *89*(C4), 6415–6426. doi: 10.1029/JC089iC04p06415

Schmelter, M. L., Hooten, M. B., & Stevens, D. K. (2011). Bayesian sediment transport model for unisize bed load. *Water Resources Research*, *47*(11), 1–15. doi: 10.1029/2011WR010754

Thorne, P. D., & Hurther, D. (2014). An overview on the use of backscattered sound for measuring suspended particle size and concentration profiles in non-cohesive inorganic sediment transport studies. *Continental Shelf Research*, *73*, 97–118. doi: 10.1016/j.csr.2013.10.017

Valipour, R., Boegman, L., Bouffard, D., & Rao, Y. R. (2017). Sediment resuspension mechanisms and their contributions to high-turbidity events in a large lake. *Limnology and Oceanography*, *62*(3), 1045–1065. doi: 10.1002/lno.10485

Zaron, E. D. (2019). Baroclinic tidal sea level from exact-repeat mission altimetry. *Journal of Physical Oceanography*, *49*(1), 193–210. doi: 10.1175/JPO-D-18-0127.1

Zulberti, A., Ivey, G. N., & Jones, N. L. (2018). Observations of Near-bed Stress beneath Nonlinear Internal Wave Trains in the Ocean. *21st Australasian Fluid Mechanics Conference*(December), 13–16.

Zulberti, A., Jones, N. L., & Ivey, G. N. (2020). Observations of Enhanced Sediment Transport by Nonlinear Internal Waves. *Geophysical Research Letters*, *47*(19), 1–11. doi: 10.1029/2020GL088499